Bubbles Formation in Helium Ion Irradiated Cu/W Multilayer Nanocomposites: Effects on Structure and Mechanical Properties

M. Callisti[a,*], M. Karlik[b], T. Polcar[a, c]

[a] National Centre for Advanced Tribology at Southampton, Faculty of Engineering and the Environment, University of Southampton, Southampton SO17 1BJ, UK

[b] Department of Materials, Faculty of Nuclear Sciences and Physical Engineering, Czech Technical University in Prague, Trojanova 13, 120 00 Prague 2, Czech Republic

[c] Department of Control Engineering, Faculty of Electrical Engineering, Czech Technical University in Prague, Technická 2, 16627 Prague 6, Czech Republic

*** Corresponding Author Information**

Dr. Mauro Callisti

M.Callisti@soton.ac.uk

Faculty of Engineering and the Environment, University of Southampton, Southampton SO17 1BJ, UK
Building 7 / Room 4027 – Mailpoint M7
Southampton, Hampshire SO171BJ
United Kingdom
Phone: +44 (0)23 8059 4438

Abstract

This study investigates the effects of He bubbles on structural and mechanical properties of sputter-deposited Cu/W multilayers. A multilayer with a periodicity of 10 nm was deposited and subjected to helium ion irradiation with two different fluences. He bubbles formed mostly in Cu layers and their distribution was affected by He concentration and radiation damage. According to SRIM calculations, in low He concentration regions bubbles formed mostly along interfaces, while more homogeneously distributed bubbles were found in Cu layers and along columnar grain boundaries in higher He concentration regions. We suggest that the capability of interfaces to annihilate point defects is weakened by the He bubbles shielding effect. Nanoindentation tests revealed a hardness decrease amounting to ~ 0.5 and ~ 1 GPa for low and high fluences, respectively. The observed softening effect is attributed to He storage-induced changes in residual stresses and columnar grain boundary/interfacial sliding facilitated by He bubbles.

Keywords: multilayers, heterostructures, interfaces, irradiation, helium bubbles, nanoindentation, transmission electron microscopy (TEM).

1. Introduction

Structural disorder and hardening effect induced by neutron and ion bombardment are being extensively studied for more than a decade [1]. Radiation can generate relevant displacement damage in metals with consequent formation of point defects, such as vacancies and interstitials and their agglomeration, to form dislocation loops, vacancy clusters and stacking fault tetrahedra [1]. The growth of vacancy clusters and their simultaneous combination with transmutation products such as helium (He), characterised by very low solubility with metals, promotes the formation of He bubbles [2]. These bubbles were found to cause swelling, radiation-hardening and dimensional instabilities in structural metals [3], which represent a real challenge for application of metals in nuclear industry both as containment vessels and fuel claddings.

It is well known that surfaces, grain boundaries (GBs) and heterointerfaces are good sinks for radiation-induced point defects and traps for implanted He [4, 5]. Composite materials with a high interface density distribution showed enhanced radiation tolerance compared to conventional single phase metals [6]. Based on this concept, several metallic multilayers produced primarily by physical vapour deposition (PVD) and by accumulative roll bonding (ARB) [7] have been used as material model systems to study the role of interfaces to reduce radiation damage. Metallic multilayers consisting of alternate nanometre-scale layers of immiscible elements [8], e.g. Cu and Nb, retained their layered structure after He-ion implantation [9]. Furthermore, when the layer thickness was lowered down to 2.5 nm He bubbles were barely observed [10]. It suggests the exceptional capability of densely distributed Cu/Nb interfaces to absorb and annihilate point defects concentration compared to bulk metals, thus limiting swelling and dimensional instabilities.

Mechanical properties of He-ion irradiated multilayers were explored mostly in relation to the periodicity (bilayer thickness), for He ion energies below 150 keV and with maximum fluences of the order of 10^{20} ions/cm^2. Radiation hardening was reported for different miscible and immiscible multilayer systems mostly with a fcc/bcc interface, such as: Cu/Nb [10, 11], Cu/V [12, 13], Fe/W [14], and V/Ag [15]. Radiation hardening in metals was attributed to the interaction of dislocations with two types of radiation-induced defects: strong obstacles (i.e. interstitials, interstitial loops, stacking fault tetrahedra and precipitates) and weak obstacles (i.e. He bubbles) [16]. In the latter case, when the layer thickness is larger than the bubbles spacing, bubble hardening effect adds to the confined layer slip (CLS) mechanism [16], thus producing a hardening effect. Conversely, when the layer thickness is comparable to the bubbles spacing, the strength is mostly determined by single dislocation crossing defect-loaded interfaces [16]. Although it is recognised that segregation of He atoms at GBs reduces the interface cohesive energy[1], the effects of He bubbles on the mechanical properties of interfaces are still to be explored and understood. The role of He bubbles, formed along interfaces, on dislocation emission and interfacial sliding (softening effect) is of particular interest.

Among the potential candidate materials referred to above, little attention has been directed to the immiscible Cu-W system, although Cu/W interfaces were suggested to be a good sink for radiation-induced point defects [17]. Cu/W multilayers, with different periodicities (10 – 50 nm) subjected to He-ion irradiation (10^{20} – 10^{21} ions/cm^{-2} at 50 keV) showed a good morphological and chemical stability and no voids were observed for a periodicity of 10 nm. However, the effects of He-ion irradiation on the mechanical properties of Cu/W multilayers are still unexplored. Therefore, this study is aimed at evaluating and correlating the effects of He bubbles formation with structural and mechanical properties of Cu/W multilayers. Moreover, the objective is also to identify possible deformation mechanisms in multilayers with He bubble-decorated interfaces. A sputter deposited multilayer with a small periodicity is used as a model material in this study to produce almost identical Cu/W interfaces with a high density distribution. The as-deposited multilayer was irradiated by He ions with different fluences and incident angles to generate damage at depths appreciable by depth-sensing nanoindentation.

2. Experimental details

A Cu/W multilayer was deposited with a nominal periodicity of $\lambda = 10$ nm and a nominal layer thickness for Cu and W of $\lambda/2$ on single crystal (100) Si wafers using a balanced magnetron sputtering apparatus (Kurt J. Lesker Company, Pennsylvania, US). The deposition was carried out for about 2 h, resulting in a total film thickness of ~ 1.15 μm. Further details regarding the deposition process are reported elsewhere [18].

Radiation experiments were performed at ambient temperature (~ 300 K) with He ion energy of 1 MeV and for two different fluences (1.1×10^{16} and 3.2×10^{16} cm^{-2}) achieved by varying the ion flux (constant exposure time). For each condition four different incidence angles (i.e. 66°, 53°, 37° and 0° between the ion beam and the normal to the target surface) were used in order to produce an as flat-profile damage distribution as possible throughout the thickness and to avoid ion channelling effects. Stopping and Range of Ions in Matter (SRIM) computer program based on Monte Carlo method [19] was used to calculate radiation damage (displacement per atom, dpa) and depth profile of He concentration in an equiatomic Cu – W compound by simulating the radiation conditions mentioned above. Threshold displacement energies of 29 eV and 71 eV were used for Cu and W [20], respectively.

The microstructure of as-deposited and irradiated multilayers was investigated by grazing incidence X-ray diffraction (XRD) by using a grazing angle of 4° with a scan step size of 0.02° over a 2θ range of 20 – 80°. Diffraction data were collected by using the Rigaku SmartLab diffraction system (Rigaku Corporation, Japan) with Cu Kα radiation, while the XRD patterns were analysed by the PDXL software together with an ICDD PDF-2 database. The structure of the as-deposited multilayer was studied by a transmission electron microscope (FEI Tecnai G2 F20 XT) operated at 200 kV. For the as-deposited multilayer, cross-sectional TEM samples were prepared by mechanical grinding and polishing followed by further thinning to an electron transparent thickness by a dual ion miller (Gatan PIPS, model 691). Structural analyses on irradiated multilayers were performed by a TEM JEM-3010 at an accelerating voltage of 300 kV. Cross-sectional TEM lamellae were prepared by the Zeiss NVision40 Focused Ion Beam (in situ lift-out), where lamellae were thinned and polished down to achieve electron transparency by mean of a Ga ion gun operated with a current of 40 pA at 30 kV.

Mechanical properties of the multilayers were measured by nanoindentation (Nano-Test Platform 4, Micro-Materials Ltd.) at ambient temperature by using a diamond Berkovich indenter. The diamond area function was calibrated before testing by using a standard fused silica sample. The indentation hardness and elastic modulus were measured for different maximum loads ranging between 0.5 and 3.5 mN to keep the maximum penetration depth around 10% of the total thickness. Each test was carried out with a constant indentation strain rate of 0.05 s^{-1}, a holding time at maximum load of 15 s and an unloading time of 5 s. Hardness and elastic modulus were evaluated from the load-displacement data by using the method outlined by Oliver and Pharr [21], assuming a Poisson ratio of 0.33. Reported values are averaged at least over 15 indents.

3. Results

3.1 As-deposited multilayer

Fig. 1 shows the XRD pattern of the as-deposited Cu/W multilayer. Both Cu (fcc) and W (bcc) layers exhibit a polycrystalline structure with W (110) and Cu (111) as the main diffraction planes. The presence of a small satellite peak at $2\theta \approx 36.5°$ suggested the formation of a weak superlattice structure [22]. The interatomic spacing (*d*) calculated for the main diffraction planes referred to the above are close to reference data (Cu: ref. 00-003-1005 and W: ref. 00-001-1204). Contrary to the results reported in other studies [23], the as-grown layers exhibited an almost stress-free condition. The structural coherent length was calculated by using the Sherrer equation, assuming a cubic shape of the crystallite domains and therefore using a shape factor of 1.06 for W (110) and of 1.15 for Cu (111). The resulting characteristic length was of ~ 5 nm for W and of ~ 7.5 nm for Cu, thus suggesting larger crystalline domains for Cu. The SAD pattern (Fig. 2a) acquired on the cross-section did not indicate any mutual preferential orientation between Cu and W nanocrystals, as only a slightly higher spot density distribution was observed along the film growth direction, thus suggesting a poorly textured multilayer structure with randomly oriented nanocrystals. It is clear from the distribution of the diffraction spots that W grains are on average much smaller than Cu grains. Careful examination of the SAD patterns showed that W (110) and Cu (111) diffraction rings were slightly stretched (i.e. 2% and 1%, respectively) along the growth direction. It suggested that both Cu and W layers were slightly compressed along the normal to the substrate, i.e. small in-plane tensile residual stress. The as-deposited multilayer exhibited a certain waviness, which became more pronounced with film growth. Observed transition from planar to wavy interfaces is attributed to the cumulative layer waviness and to the shadowing effect inherent to the deposition process [18].

The as-deposited multilayer consisted of a columnar structure extended throughout the entire coating thickness. Columns exhibited an average diameter of ~ 20 nm, although occasionally larger columns formed owing to competitive grow mechanism (Fig. 2b). In some cases, where pronounced layer curvature is observed, columnar grain boundaries were found to consist of nano-crystals (~ 5 nm in size, Fig. 2b) embedded in an amorphous channel. W layers exhibited a nano-columnar structure consisting of 1 – 3 nm wide columnar grains extended throughout the layer thickness (4 – 5 nm) and separated each other by veins with a less dense structure. On the other hand, Cu layers exhibited larger grains extended throughout the layer thickness (~ 15 nm wide and ~ 5 nm thick). In Cu layers bent atomic planes were observed together with edge dislocations close to the interfaces (Fig. 2c). W-on-Cu interfaces were much smoother and sharper compared to Cu-on-W interfaces (Fig. 2d). A similar structure was reported for electron beam evaporated Cu/W multilayers [24]. W-on-Cu interfaces showed a higher interfacial coherency (Fig. 2c and 2d) likely responsible for the observed satellite peak found in the XRD pattern (Fig. 1). Observed asymmetric interfaces are attributed to the different energetic state of W and Cu adatoms during layers growth, W adatoms having a limited mobility [18]. W layers grew on a much more regular and flat Cu substrate and beside the overall waviness, sharp W-on-Cu interfaces formed as shown in Fig. 2d. Conversely, owing to the jagged surface exhibited by W layers, a more complex scenario was observed for Cu-on-W interfaces. In fact, Cu layers, at least in the early stage of growth, exhibited an irregular structure with high defect density distribution. Since growing Cu structure has to adapt to a geometrically more complex substrate, generated Cu-on-W interfaces exhibit a large amount of defects. Further deposition of copper resulted in a more regular structure (Fig. 2d).

3.2 SRIM calculations

Fig. 3 shows the projected He concentration profile and the radiation damage (obtained as sum of partial profiles for each incidence angles), in relation to depth and fluences calculated by SRIM on equiatomic Cu – W alloy target by using the detailed calculation with full damage cascade. He concentration peak shifted closer to the surface for larger incident angles. The resulting concentration profile suggests that a concentration peak should be localised at a depth of about 800 – 900 nm underneath the free surface, although such peak exhibited a certain broadening. About 3 times higher He concentration is produced with high fluence ($3.2 \times 10^{16} cm^{-2}$). The peak damage induced by helium collisions in the compound approaches ~ 2.2 dpa at a depth below ~ 600 nm for low fluence, while it approaches ~ 6.5 dpa at a depth ranging between 700 nm and 1 μm for high fluence. A Cu/W multilayer with a periodicity of 100 nm ($t_{Cu} = t_W$) and a thickness of 1.1 μm was also simulated by SRIM in order to gather more insight about the response of a layered structure to radiation damage. He concentration profiles and radiation damage (not shown) obtained for the multilayer were very similar to those shown in Fig. 3; however, target atoms displacement and vacancies per ion were much higher in Cu layers as expected.

3.3 Structure after irradiation

Fig. 1 shows the XRD pattern of the multilayer irradiated with different fluences. The satellite peak observed for the as-deposited multilayer at $2\theta \approx 36.5°$ was not found for the irradiated samples, which might suggest structural changes at the interfaces or in the constituent layers [25]. In order to highlight possible peaks intensity evolutions, the XRD patterns of irradiated samples were normalised with respect to the XRD pattern of the as-deposited multilayer. No appreciable peak intensity evolution in relation to the irradiation conditions was observed. On the other hand, the W pattern, contrary to the Cu pattern, shifted toward higher 2θ angles in relation to the fluence (Fig. 1). Changes in residual stresses were therefore produced, especially in the W layers, and intensified with fluence.

Helium irradiation experiments, even with high fluence, did not cause any appreciable change on the top surface of the films compared to their as-deposited condition and the columnar structure could still be clearly distinguished after irradiation, as shown in Fig. 4. SEM images of the as-deposited sample replicate Fig. 4 and therefore were not reported.

Cross-sectional TEM analyses showed that the layered structure was retained after irradiation with low fluence as shown in Fig. 5a. Gas-filled small cavities are easily discernible by acquiring out-of-focus TEM images due to Fresnel contrast [26]. The SAD pattern (inset in Fig. 5a) acquired on the entire cross-section corroborated the XRD analyses suggesting no structural changes in Cu and W layers. In addition to the porous structure between columns, porosity parallel to the Cu/W interfaces (highlighted by arrow in Fig. 5a) was observed at the calculated He concentration peak position, as also found elsewhere [27]. The observed brighter feature parallel to interfaces could be due to a large He pocket or to interfacial detachment of the layers due to excessive He accumulation.

According to the calculated He concentration profile (Fig. 3), TEM observations were conducted primarily in high and low He concentration regions. In the latter case, bright field TEM images acquired under different focus conditions (not reported) did not show any feature attributable to He bubbles, thus suggesting that He concentration close to the surface was too low to form He bubbles detectable by TEM. Fig. 6 shows the atomic structure of the multilayer at a depth of ~ 300 nm underneath the film surface. No relevant signs of amorphisation induced by ion implantation were observed and the semi-coherent nature of the interface was preserved.

In the high He concentration regions (in the sample irradiated with low fluence), densely distributed He bubbles formed mostly in the Cu layers (Fig. 5b). These bubbles were often observed to form close and along interfaces but mostly within the Cu layers, as highlighted by arrows in Fig. 5b. Detail shown in Fig. 5c demonstrates that the average bubble size is smaller than $t_{Cu}/2$ (out-of-focus images alter the actual size of features). Infrequently, bubbles were also observed to form agglomerations in Cu layers as shown in Fig. 5d, which might indicate bubbles growth, impingement and eventually coalescence [28].

After irradiation with high fluence, the layered structure was retained (Fig. 7a) and, based on the SAD patterns analysis, no significant changes in crystal structure were found for the constituent layers. In this case, He bubbles also formed close to the coating surface (highlighted in Fig. 7b). Around the calculated He concentration peak, He bubbles of a similar size as those formed at low fluence also populated the inner part of Cu layers (Fig. 7c) contrary to the case with low fluence (Fig. 5), where bubbles formed mostly close to interfaces. Occasionally, bubbles extended to W layers through interfaces (highlighted in the area closer to the substrate in Fig. 7c).

Boundaries between columns may represent, owing to their less dense structure, easy diffusion paths for interstitials and He ions. Furthermore, local interconnections between Cu layers at the columnar grain boundaris (Fig. 2b) can further enhance diffusion through layers. He bubbles were clearly observed along columnar grain boundaries mostly within Cu layers and only occasionally in W layers as highlighted in Fig. 7c.

3.4 Mechanical properties

Fig. 8 summarises mechanical properties of the as-deposited and irradiated multilayers as a function of the radiation fluence. Mechanical properties of the as-deposited multilayer were evaluated from a linear fit extrapolation for zero load using experimental data acquired for a load ranging between 2 – 3.5 mN. The pristine multilayer exhibited a hardness of 5.7±0.1 GPa and an elastic modulus of 142±10 GPa, close to values reported by Monclus et al. [18]. For loads ≤ 1.5 mN (depths below ~ 70 nm), indentation size effect was observed for all multilayers; therefore, only data acquired with higher load was used to evaluate hardness and elastic modulus. Fig. 8a shows a hardness plateau for loads above 2 mN (depths ≥ 80 nm); conversely, hardness of irradiated samples was affected both by the indentation depth and radiation fluence. Based on the hardness plateau found for the as-deposited multilayer for loads ≥ 2 mN, it is expected that the small variation in indentation depth for any specific load (Fig. 8c) does not have any relevant effect on the corresponding hardness. Therefore, hardness variations measured at indentation depths between 80 – 100 nm (about 10% of the coating thickness) are attributed to different levels of radiation damage (Fig. 3). The elastic modulus (Fig. 8b) of the multilayer irradiated with low and high fluence was 138±8 and 129±10 GPa, respectively.

4. Discussion

4.1 Structural changes after irradiation

In spite of the asymmetric interfacial structure, the multilayer exhibited some evidence of superlattice arrangement documented by the satellite peak in Fig. 1. After irradiation, regardless of the radiation fluence, the satellite peak vanished. The absence of satellite peaks in multilayers can be attributed to different structural and geometrical aspects, such as: interfacial mixing, thickness fluctuation of each individual layer, when one or both constituent elements are amorphous or when the boundary layer is amorphous [25]. The Cu-W system with an equiatomic composition has a positive heat of mixing ($\Delta H = + 36$ kJ calculated by the Miedema's model [29]), denoting a high immiscibility both in liquid and solid state. Intermixing induced by ballistic effects can be possible between immiscible elements at very low temperatures [29]. However, when the temperature is raised above a certain threshold, a demixing phenomenon occurs due to the influence of the chemical potential gradient, where atoms in the mixed layer segregate back in their original layer through, likely, an interstitial migration mechanism. It was reported for a Cu/W multilayer ($\lambda = 10$ nm) that the contribution of thermodynamically driven forces opposing ballistic effects was relevant even when small and weakly energetic cascades were formed [30]. This effect was more prominent in Cu layers owing to the longer lifetime of the thermal spike generated in Cu, thus encouraging a temperature-like mobility [29]. The demixing mechanism mentioned above was deducted by conducting irradiation experiments at low temperatures (below 100 K) with subsequent annealing at ambient temperature. These results suggest that the formation of a mixed layer at the Cu/W interfaces is highly unlikely in the case under investigation, where an estimated temperature of ~ 350 K was experienced by the sample during irradiation.

The full width at half maximum (FWHM) for both W (110) and Cu (111) peaks did not exhibit noticeable changes after irradiation and interface intermixing or layer amorphisation was ruled out. Therefore, the presence of bubbles along interfaces should be the most probable reason behind the absence of satellite peaks for irradiated multilayers.

Interestingly, only the W pattern exhibited a progressive shift toward higher 2θ angles in relation to the radiation fluence (Fig. 1). This incoherent change in residual stress is attributed to the predominant formation of He bubbles in Cu layers (Fig. 5 and 6). Prominent accumulation of helium changed the size of Cu layers without affecting significantly its atomic structure. On the other hand, this expansion generated tensile stress in the W layers especially for high fluence.

4.2 He bubbles formation and distribution

It is generally observed that under energetic He^+ implantations, vacancies and interstitials are formed in the collision cascades. In view of the very low solubility of He in metals and of its strong binding energy with vacancies, implanted He precipitates into vacancy clusters that grow into He bubbles [2]. The predominant formation of He bubbles in Cu rather than in W can be attributed to several factors. The vacancy formation energy E_f for Cu (1.27 eV) is about three times lower than that for W (3.8 eV) [31]; therefore, less vacancy clusters are available in W layers as nucleation sites for He bubbles. Furthermore, vacancies formed in Cu have a migration energy E_m (0.8 eV) and activation energy for self-diffusion E_{sd} (2.07 eV) much lower compared to those for W (E_m = 1.8 and E_{sd} = 5.7 eV) [31]. It was reported that bubble growth could be enhanced by vacancies and/or He diffusion in relation to the homologous temperature [32]. Based on the much higher thermodynamic melting temperature of W compared to Cu and the consequent homologous temperature almost three orders of magnitude higher for W, vacancies and He atoms are expected to have a considerably higher mobility in Cu than in W. The average number of jumps made by vacancies in bulk metals can be estimated by [32]:

$$n = A\, z\, v\, t\, e^{-\frac{E_m}{k T_a}} \qquad (1)$$

where A is a constant (≈ 1) involving the entropy of migration, z is the coordination around a vacancy, v is the Debye frequency ($\approx 10^{13}$ /s), t is the annealing time at the ageing temperature T_a and E_m is the migration energy of the defect. Assuming a reference annealing time (intended as heating during irradiation) of 1 h and an estimated temperature during radiation experiments of ~ 350 K, single vacancies would migrate an average distance ($\sqrt{n} \times atomic\ spacing$) of ~ 3 nm in Cu, whereas vacancy migration would be negligible in W.

As a conclusion based on the previous considerations, vacancies requires much more energy to form in W. Once formed, they remain as single vacancies (no vacancy clusters formation) with almost no diffusivity at 350 K, even after several hours of annealing. On the other hand, vacancies form more easily in Cu and can diffuse relatively long distances (~ 8 a_{Cu}) to form clusters and therefore He bubbles. Consequently, a significantly larger amount of bubbles is formed in bulk Cu. Gonzalez et al. [33] used density functional theory (DFT) calculations to show tendency of both vacancies and helium atoms to reach Cu/W interfaces; furthermore, they showed that the helium-vacancy complex is likely to form at the Cu/W interface, especially inside the Cu layers.

Interfaces and grain boundaries (GBs) promoted heterogeneous bubbles formation affecting the bubbles distribution within layers. In fact, He bubbles were found to form first along interfaces in Cu layers (Fig. 5 and 7).

It was reported that different interface structures have different capabilities to sink point defects [1, 5, 34]. As shown in Fig. 2d and discussed in section 3.1, W-on-Cu and Cu-on-W interfaces exhibited rather different morphological and structural properties. However, He bubbles formed equally at both interfaces (Fig. 5 and 7), thus suggesting no dominant sink site between Cu-on-W and W-on-Cu interfaces. He bubbles formed also along boundaries between columns (Fig. 7c).

For the high fluence, He bubbles formed closer to the film surface (Fig. 7a) and a higher bubble density distribution was observed at the bottom of the coating (Fig. 7c). Combining experimental evidence (TEM analysis of bubbles) and SRIM calculations (Fig. 3), a He concentration of ~ 7 % (corresponding to ~ 2 dpa) is sufficient to cause He bubble nucleation and growth up to a size observable by TEM, while He concentrations below ∼5 % (dpa below ~ 1.5 dpa) is too low to form He bubles of a size appreciable by TEM. Therefore, the minimum He concentration, where He bubbles can be observed in this Cu/W multilayer, lays between 5 – 7 % (dpa > 1.5).

In the sample irradiated with high fluence, two different He bubbles distributions were observed across the film thickness. Close to the film surface (He concentration ∼ 6 – 10 %) He bubbles formed mostly along interfaces (Fig. 7b). On the other hand, in high He concentration regions (He concentration > 20 % and dpa > 5) formation of homogeneously distributed He bubbles in Cu layers (Fig. 7c) occurred. At first instance, these differences could be attributed to the heavier radiation damage (Fig. 3) and therefore to the larger amount of nucleation sites made available within the layers under the high fluence.

Trinkaus et al. [35] reported that at low temperature the dominant nucleation mode of He bubbles (homogeneous vs. heterogeneous), is determined by the relation between the sink strenght of bubble nuclei and the sink stength of pre-existing traps (precipitates, interfaces, defects). For a given sink strenght of a pre-exsting trap, homogeneous nucleation tends to domante at low temperature and/or high He production rates.

In this study, a more homogeneous He bubbles nucleation was expected to occur in the sample irradiated with higher flux. However, for high fluence (higher flux), different He bubbles distributions were observed (Fig. 7). Therefore, for a given flux, the nucleation and distribution of He bubbles in Cu layers is affected by the He concentration and/or radiation damage. Furthermore, according to our observations (Fig. 5 and Fig. 7), there were no appreciable difference in bubbles size for different fluxes; it indicates that a heavier radiation damage encourages formation of more bubbles rather then appreciable growth of existing bubbles. These results lead to the conclusion that the sink efficiency of interfaces to absorb vacancies can be lowered by progressive He segregation. Consequently, vacancies in the grain interior are not absorbed at interface and hence act as seeds promoting He bubbles formation with homogenous distribution in Cu layers. Therefore, heterogeneous bubble formation can be expected as long as the interfaces are not heavily populated by He bubbles. It also suggests that the positive role of interfaces to store implanted helium can be hindered once they are shielded by He bubbles.

4.3 Post-irradiation softening

Microstructural changes after helium implantation were such to produce a softening effect, which amounted to a maximum of ~ 0.5 GPa (9%) and ~ 1 GPa (18%) for low and high fluence (Fig. 8a), respectively. Here, we attempt to rationalise how hardness of irradiated Cu/W multilayers could be affected by the synergetic effect of different structural factors, namely residual stress changes and He bubbles formation at interface/grain boundary and/or in the grain interior.

In nanocrystalline metals, grain boundary sliding and dislocations gliding are the key factors affecting deformation mechanisms and strength [31] and their alteration have significant effects on the resulting mechanical behaviour. Formation of He bubbles both at interfaces and in the grain interior have opposite effects on strength. Bubbles formed in the grain interior pin dislocations traversing the grains with a corresponding hardening effect [16]. On the other hand, when He bubbles form at interfaces, the beneficial role of interfaces is hindered and dislocation emission and interfacial sliding is facilitated with a consequent softening effect [15]. Furthermore, even in the case where He atoms are only segregated at interfaces as impurities, the interface cohesive strength is significantly reduced [36].

With particular regard to non-irradiated Cu/W interfaces, it was reported that, under compression, copper is squeezed in the GBs of W nano-grains [18], thus affecting hardness. Such phenomenon was ascribed to the jagged Cu-on-W interface beside the mismatch in mechanical properties between constituent elements. Due to the jagged Cu-on-W interfaces (Fig. 2d), a similar mechanism can be expected in the Cu/W multilayer reported in this study. Following irradiation experiments, the formation of nearly continuous bubble chains at interfaces may cause a “bubble bearing effect” between layers, which facilitates interface sliding under load. A complex scenario comes into picture when bubbles form both at GBs and in the grains interior; the resulting deformation behaviour would be governed by the less energetically demanding mechanism.

Mechanical properties of sputter-deposited thin films are also affected by residual stresses inherent the deposition process and/or caused by post-deposition treatments. Typically, compressive residual stresses contribute at increasing indentation hardness of sputter-deposited thin films [37].

For low fluence, XRD analyses did not reveal any change in interatomic spacing and coherent length for Cu and W with respect to their as-deposited condition. Therefore, change in residual stresses is ruled out as the possible cause affecting hardness. Experimental observations documented in Fig. 5 and Fig. 7 indicate that the formation of discontinuous chains of pressurised He bubbles [16] at Cu-on-W interfaces could limit the squeezing effect of Cu in W layers, thus generating in fact a hardening effect. Discontinuous bubble chains along interfaces as well as bubbles formed at columnar grain boundaries encourage Cu/W interface and GBs sliding (softening effect). Based on the results shown in Fig. 8a, bubble hardening effect in Cu grains and hardening generated by limited squeezing effect is counterbalanced by interfacial sliding, thus resulting in relatively small changes in hardness (~ 0.5 GPa).

For high fluence, three factors act simultaneously: (i) facilitated W-on-Cu and columnar GBs sliding, (ii) tensile residual stress in W layers and (iii) bubble hardening effect in the grains interior. The first two mechanisms contribute to decrease hardness, while (iii) produces a hardening effect. For high fluence interfacial sliding is further enhanced, which, combined with the tensile stress formed in W layers, resulted in a more pronounced decrease in hardness (Fig. 8a).

In order to shed light on the deformation mechanism of He bubbles-filled multilayers, a plastically deformed multilayer (irradiated with high fluence) after nanoindentation test was subject to TEM studies. Indentation was performed at a maximum depth of ~ 500 nm with a corresponding residual depth of ~ 300 nm. The cross-sectional TEM image in Fig. 9a shows an overview of the layered structure underneath the indented surface. The larger circular dashed line delineates roughly the volume of material permanently deformed during indentation. The dashed lines in Fig. 9a show that columnar grains located away from the loading axes deformed to accommodate the load, see detail in Fig. 9e. Shear deformation, facilitated by the presence of He bubbles along GBs (see Fig. 7c), took place between adjacent columnar grains (see Fig. 9e). Layers located in tilted columnar grains (highlighted in Fig. 9e) retained interfaces parallel to those located in non-tilted regions of the columns (see structure closer to the substrate in Fig. 9). As no cracks were observed by TEM in the volume of material interrogated by nanoindentation (accordingly no discontinuities were found on the load-displacement curves), it suggests that facilitated interfacial sliding occurred under load. According to SRIM calculations, the interfacial sliding highlighted in Fig. 9e occurred at a depth where He concentration was just above the threshold concentration required for He bubbles observation (see section 4.2).

Along the loading axis the shear deformation was very limited and layers were compressed perpendicularly to the interfaces. Fig. 9b shows that the first few layers were mixed and followed by discontinuous W and Cu layers. Interestingly, the compressive stress generated during indentation flattened the layered structure making it less wavy compared to the as-deposited morphology (Fig. 9c), and no squeezing effects of Cu in W were observed. At a certain depth below the indented surface (point d in Fig. 9a), the layered structure retained most of its waviness (Fig. 9d) as in the as-deposited state.

These results show possible undesirable effects accompanying He bubbles formation and highlight some of the aspects still unexplored or not well understood regarding the formation of He bubbles in layered structures. Although the preferential segregation of He atoms along interfaces and grain boundaries has beneficial effects on limiting swelling and dimensional instabilities, simultaneously the role of interfaces to annihilate point defects and to guarantee mechanical strength can be weakened. Therefore, further studies combining large scale atomistic simulations with relevant experiments are needed in this direction in order to provide comprehensive understating on the role of He bubbles and of the segregation of helium at interfaces and GBs on structural and mechanical performance of layered structures.

5. Conclusions

Structural and mechanical properties of a sputter deposited Cu/W multilayer nanocomposite subjected to helium irradiation were investigated in relation to the helium concentration. Helium bubbles formed mostly in Cu layers and along columnar grain boundaries with a density distribution affected by the helium concentration and radiation damage. In low concentration regions, heterogeneous bubbles formation occurred in the Cu layers mostly with interfaces decorated by bubbles chains. On the other hand, bubbles formed more homogenously in the Cu layers and at columnar grain boundaries in regions with high helium concentration. We suggest that the efficiency of interfaces to annihilate radiation-induced point defects is hindered by the shielding effect of helium bubbles. A progressive decrease in mechanical properties, in relation to the helium concentration, was attributed to residual stress variations caused by stored helium and to the lower cohesive strength of bubbles-populated interfaces and grain boundaries.

Acknowledgement

The authors express their gratitude to the European Commission for financial support through the project RADINTERFACES (Grant agreement no. 263273). The ‘South of England Analytical Electron Microscope’ (EPSRC Grant code EP/K040375/1) is acknowledged for access to the electron microscopy facilities.

References

[1] I.J. Beyerlein, M.J. Demkowicz, A. Misra, B.P. Uberuaga, Prog. Mater. Sci. 74 (2015) 125-210.

[2] Q. M. Wei, Y. Q. Wang, M. Nastasi, A. Misra, Philos. Mag., Vol. 91, No. 4, 2011, 553-573.

[3] F. A. Garner, M. B. Toloczko, B. H. Sencer, J. Nucl. Mater. 276 (2000) 123.

[4] X.-M. Bai, A. F. Voter, R. G. Hoagland, M. Nastasi, B. P. Uberuaga, Science, Vol. 327, 2010.

[5] M. J. Demkowicz, A. Misra, A. Caro, Curr. Opin. Solid State Mater. Sci. 16 (2012) 101-108.

[6] A. Misra, M. J. Demkowicz, X. Zhang, R. G. Hoagland, JOM, September 2007.

[7] I. J. Beyerlein, A. Caro, M. J. Demkowicz, N. A. Mara, A. Misra, B. P. Uberuaga, Mater. Today, Vol. 16, No. 11, 2013.

[8] M. J. Demkowicz, R. G. Hoagland, J. P. Hirth, Phys. Rev. Lett., PRL 100, 136102 (2008).

[9] T. Hochbauer, A. Misra, K. Hattar, R. G. Hoagland, J. Appl. Phys. 98, 123516 (2005).

[10] X. Zhang, N. Li, O. Anderoglu, H. Wang, J. G. Swadener, T. Hochbauer, A. Misra, R. G. Hoagland, Nucl. Instrum. Methods Phys. Res., Sect. B 261 (2007) 1129-1132.

[11] K. Hatter, M. J. Demkowicz, A. Misra, I. M. Robertson, R. G. Hoagland, Scripta Mater. 58 (2008) 541-544.

[12] E. G. Fu, J. Carter, G. Swadener, A. Misra, L. Shao, H. Wang, X. Zhang, J. Nucl. Mater. 385 (2009) 629-632.

[13] E. G. Fu, A. Misra, H. Wang, L. Shao, X. Zhang, J. Nucl. Mater. 407 (2010) 178-188.

[14] N. Li, E. G. Fu, H. Wang, J. J. Carter, L. Shao, S. A. Maloy, A. Misra, X. Zhang, J. Nucl. Mater. 389 (2009) 233-238.

[15] Q. M. Wei, N. Li, N. Mara, M. Nastasi, A. Misra, Acta Mater. 59 (2011) 6331-6340.

[16] N. Li, M. Nastasi, A. Misra, Int. J. Plast. 32-33 (2012) 1-16.

[17] Y. Gao, T. Yang, J. Xue, S. Yan, S. Zhou, Y. Wang, D. T. K. Kwok, P. K. Chu, Y. Zhang, J. Nucl. Mater 413 (2011) 11-15.

[18] M. A. Monclus, M. Karlik, M. Callisti, E. Frutos, J. LLorca, T. Polcar, J. M. Molina-Aldareguia, Thin Solid Films 571 (2014) 275-282.

[19] Ziegler J., 2011. The Stopping and Range of Ions in Matter (SRIM), http://www.srim.org.

[20] J. Pacaud, C. Jaouen, G. Gladyszewski, J. Appl. Phys. Vol. 86, No. 9, 1999.

[21] W.C. Oliver, G.M. Pharr, J. Mater. Res., 19 (1) (2004), p. 3.

[22] B. M. Clemens, J. G. Gay, Phys. Rev. B, Vol.35, 17, (1987), 9337-9340.

[23] B. Girault, P. Villain, E. Le Bourhis, P. Goudeau, P.-O. Renault, Surf. Coat. Technol. 201 (2006) 4372-4376.

[24] S. P. Wen, R. L. Zong, F. Zeng, Y. Gao, F. Pan, Acta Mater. 55 (2007) 345-351.

[25] W. Liu, A. Hu, S.-S. Jiang, Y. Qiu, W.-H. Liu, Z. Q. Wu, J. Phys.: Condens. Matter 1 (1989) 8771-8778.

[26] J.-F. Barbot, F. Pailloux, M.-L. David, L. Pizzagalli, E. Oliviero, G. Lucas, J. Appl. Phys.104, 043526 (2008).

[27] O. Anderoglu, M. J. Zhou, J. Zhang, Y. Q. Wang, S. A. Maloy, J. K. Baldwin, A. Misra, J. Nucl. Mater. 435 (2013) 96-101.

[28] G. Gutierrez, S. Peuget, J. A. Hinks, G. Greaves, S. E. Donnelly, E. Oliviero, C. Jegou, J. Nucl. Mater. 452 (2014) 565-568.

[29] A. R. Miedema, Philips Tech. Rev. 36, 217 (1989).

[30] J. Pacaud, G. Gladyszewski, C. Jaouen, A. Naudon, Ph. Goudeau, J. Grilhe, J. Appl. Phys. 73 (6), (1993).

[31] R. E. Smallman, R. J. Bishop, Moden Physical Metallurgy and Materials Engineering, sixth ed., Linacre House, Jordan Hill, Oxford (UK), 1999.

[32] L.J. Perryman,P.J. Goodhew, J. Nucl. Mater. 165 (1989) 110.

[33] C. Gonzalez, R. Iglesias, Materials and Design, 91 (2016) 171-179.

[34] W. Z. Han, M. J. Demkowicz, E. G. Fu, Y. Q. Wang, A. Misra, Acta Mater. 60 (2012) 6341-6351.

[35] H. Trinkaus, B. N. Singh, J. Nucl. Mater. 323 (2003) 229-242.

[36] R. W. Smith, W. T. Geng, C. B. Geller, R. Wu, A. J. Freeman, Scripta Mater. 43 (2000) 957-961.

[37] R. Daniel, A. Zeilinger, T. Schoberl, B. Sartory, C. Mitterer, J. Keckes, J. Appl. Phys. 117, 235301 (2015).

Figure captions

Fig. 1 – XRD patterns of as-deposited and He^+ irradiated Cu/W multilayers.

Fig. 2 – Cross-sectional TEM (XTEM) images of the as-deposited Cu/W multilayer. (a) Selected area electron diffraction pattern (SADP); (b) columnar grain boundary consisting of crystalline domains embedded in an amorphous structure; (c) W-on-Cu interface: bending of Cu atomic planes and edge dislocations are observed close to the interface; (d) asymmetric nature of Cu/W interfaces: W-on-Cu interfaces are sharp and flatter compared to Cu-on-W interfaces, which exhibit a disordered structure with high defect density distribution.

Fig. 3 – SRIM calculations of the He concentration profiles and radiation damages (dpa) vs. depth in W-Cu equiatomic alloy for two different fluences: 1.1×10^{16} and 3.2×10^{16} cm^{-2}.

Fig. 4 – SEM image of the Cu/W top surface after He ion irradiation with high fluence.

Fig. 5 - Cross-sectional TEM (XTEM) images of the Cu/W multilayer irradiated with low fluence. (a) BF TEM image of the bottom part of the multilayer where the He concentration peak is expected based on SRIM calculations. The arrow highlights porosity parallel to the interfaces. (b) Underfocused TEM image in the region around the He concentration peak. The arrows highlight He bubbles formed along interfaces. (c) Enlargement of the window *C* in (b) giving details about the He bubbles distribution within Cu and W layers. (d) Underfocused TEM image of the region around the He concentration peak showing agglomerations of He bubbles in the Cu layers.

Fig. 6 – HR-TEM image of the Cu/W multilayer irradiated with low fluence at a depth of about 300 nm below the top surface.

Fig. 7 - Cross-sectional TEM (XTEM) images of the Cu/W multilayer irradiated with high fluence. (a) BF TEM image of the bottom part of the multilayer where the He concentration peak is expected based on SRIM calculations. (b) Underfocused TEM image in the region close to the top surface showing He bubbles formation along interfaces, as highlighted by arrows. (c) Underfocused TEM image in the region close to the substrate showing random formation of He bubbles in the Cu layers and occasionally in W layers. He bubbles formed also along the columnar grain boundary (GB).

Fig. 8 – Mechanical properties measured by nanoindentation on as-deposited and irradiated Cu/W multilayers. (a) Hardness vs. load; relevant information about indentation depth are reported on the figure. (b) Young's modulus calculated assuming a Poisson's ratio of 0.33 (dashed lines correspond to the linear fitting used to estimate the elastic modulus of each multilayer as reported in the text). (c) Average maximum penetration depth in relation to the indentation load.

Fig. 9 – Cross-sectional BF TEM images of the plastically deformed Cu/W multilayer irradiated with high fluence: (a) overview of the structure underneath the indented surface (SAD pattern in the inset) and indication of the locations where detail micrographs were collected; (b) detail of the layered structure at the free surface; (c) structure ~ 100 nm below the free surface; (d) layered structure at about half thickness and (e) detail of the layered structure along the side of the indent. A schematic representation of the Berkovich tip is reported in all micrographs.

Figures

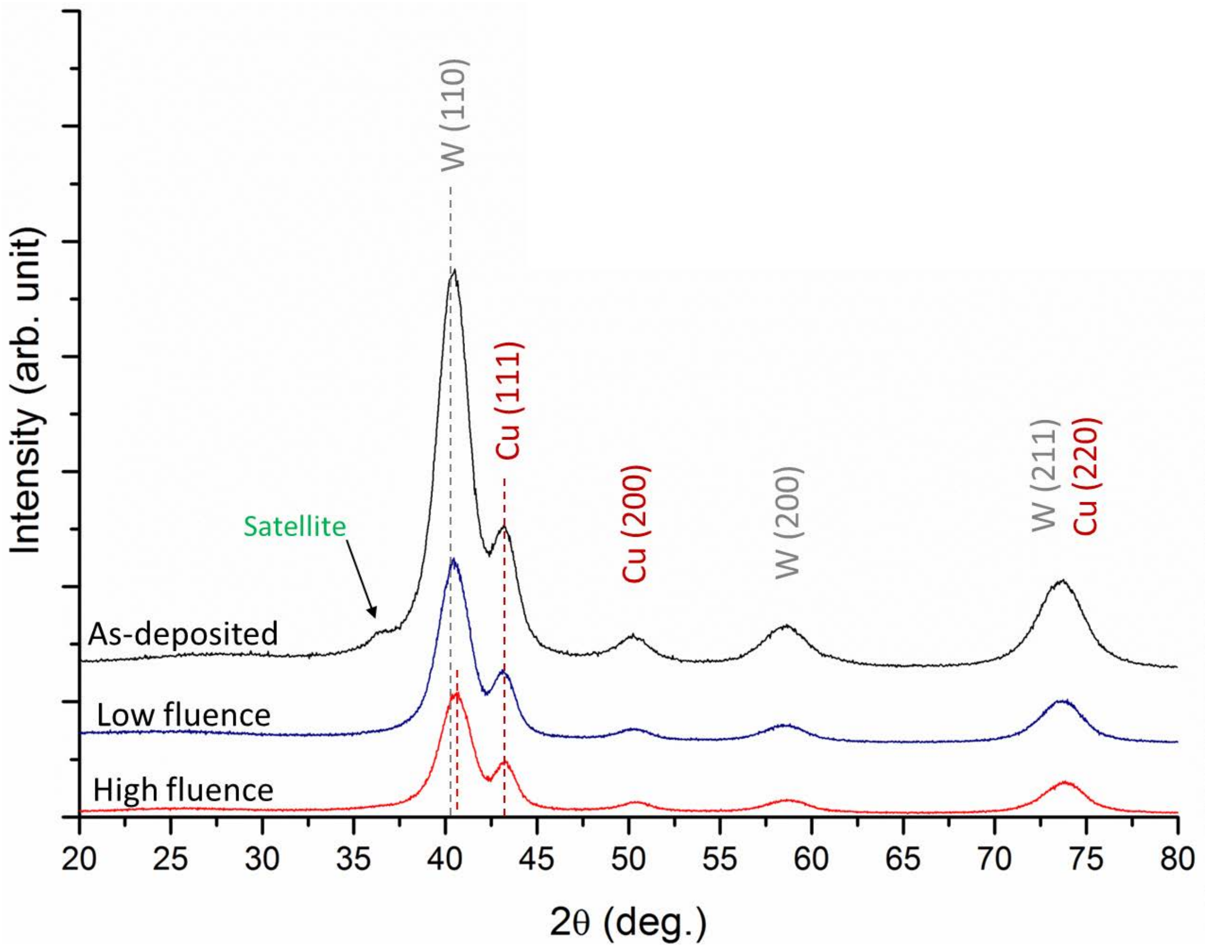

Fig. 1

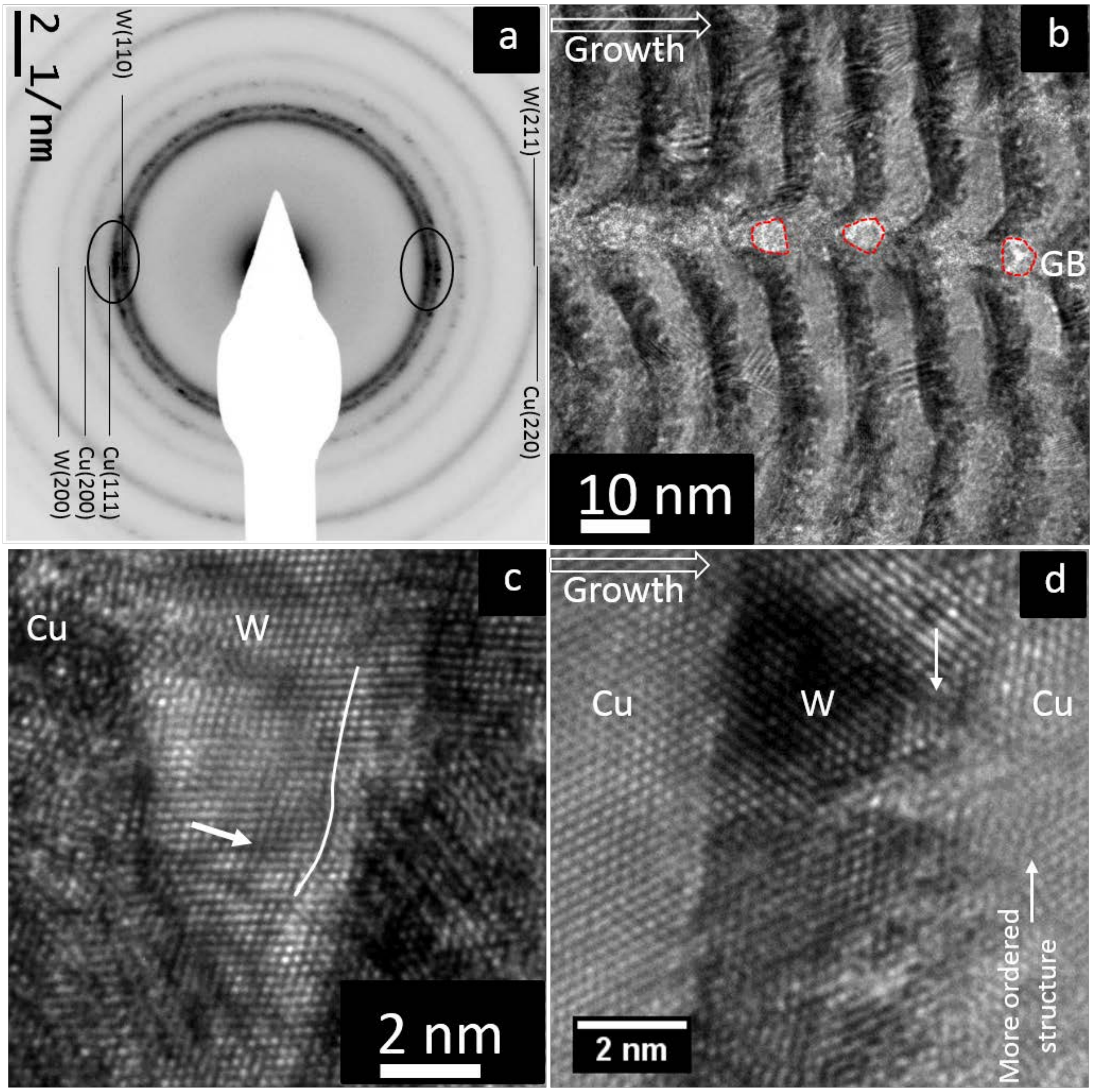
a
2 1/nm
W(110)
W(211)
Cu(220)
Cu(111)
Cu(200)
W(200)
b
Growth
GB
10 nm
c
Cu
W
2 nm
d
Growth
Cu
W
Cu
2 nm
More ordered structure

Fig. 2

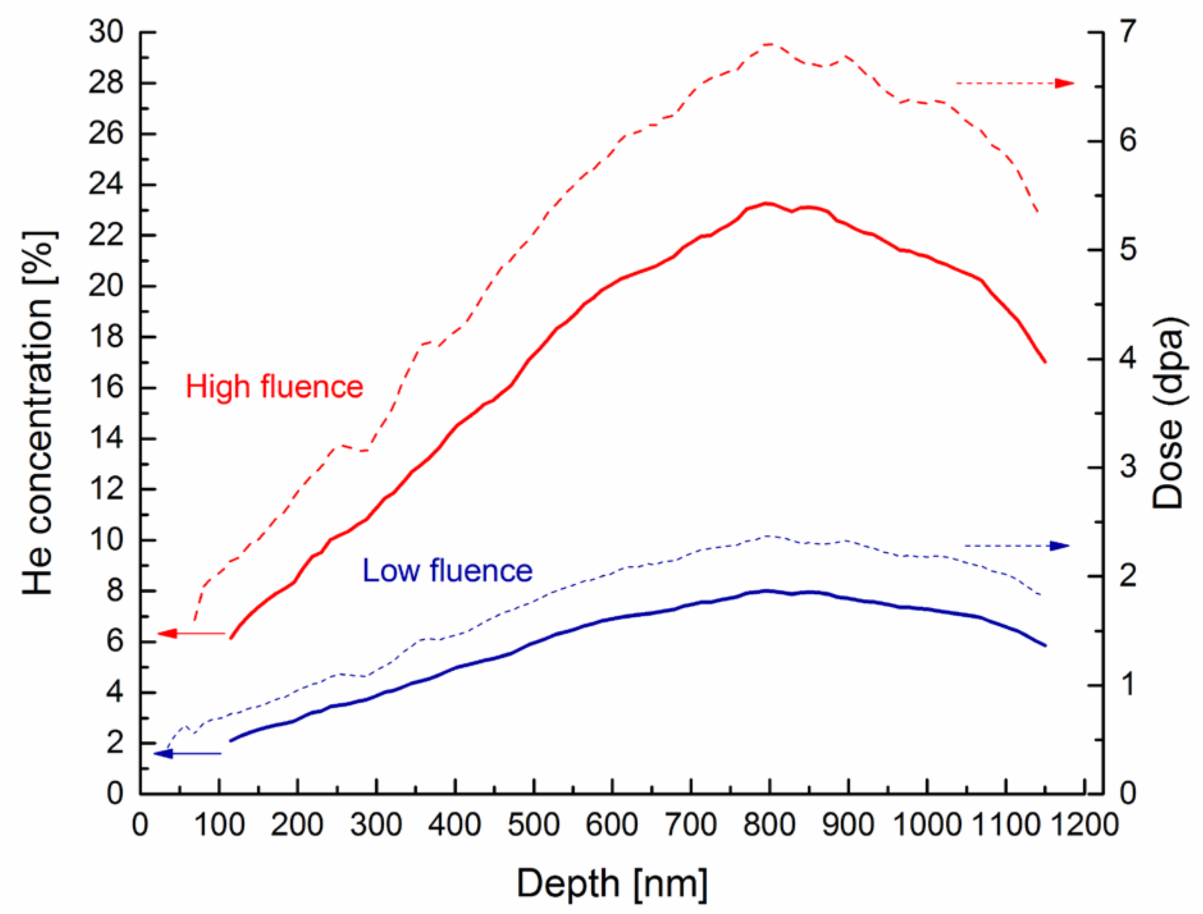
He concentration [%]
Dose (dpa)
Depth [nm]
High fluence
Low fluence
0
2
4
6
8
10
12
14
16
18
20
22
24
26
28
30
0
1
2
3
4
5
6
7
0
100
200
300
400
500
600
700
800
900
1000
1100
1200

Fig. 3

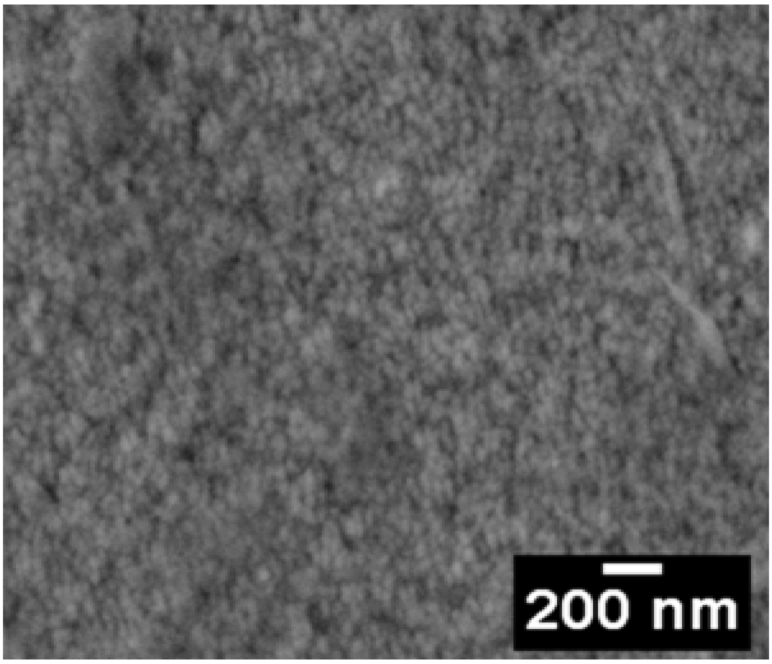
200 nm

Fig. 4

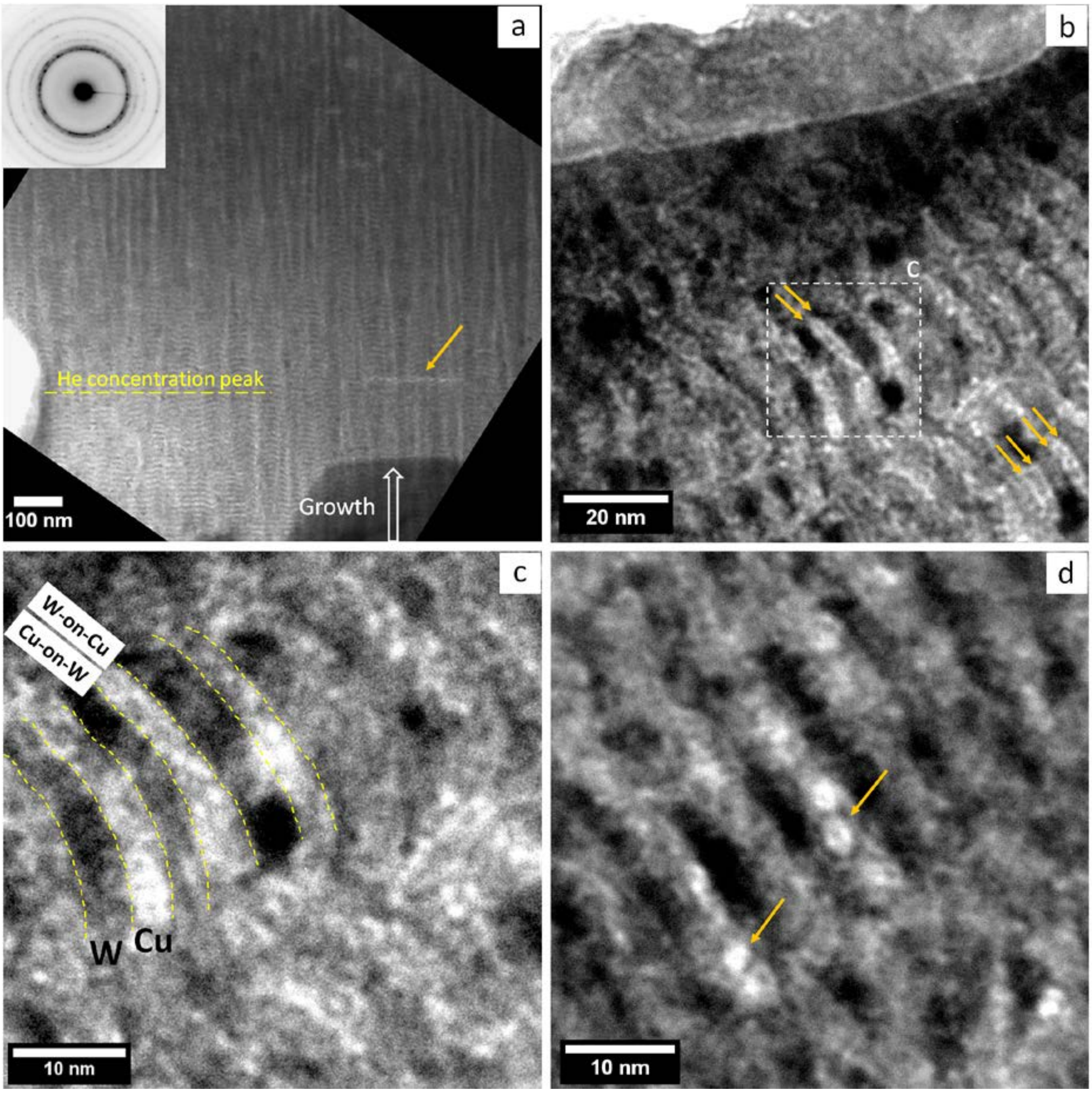
a
He concentration peak
Growth
100 nm
b
c
20 nm
c
W-on-Cu
Cu-on-W
W
Cu
10 nm
d
10 nm

Fig. 5

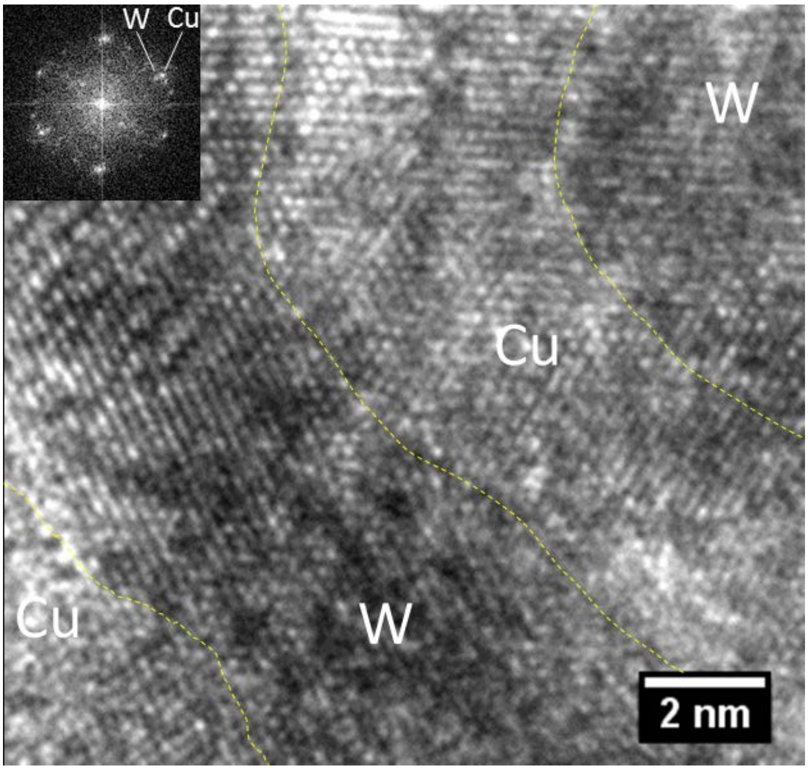

Fig. 6

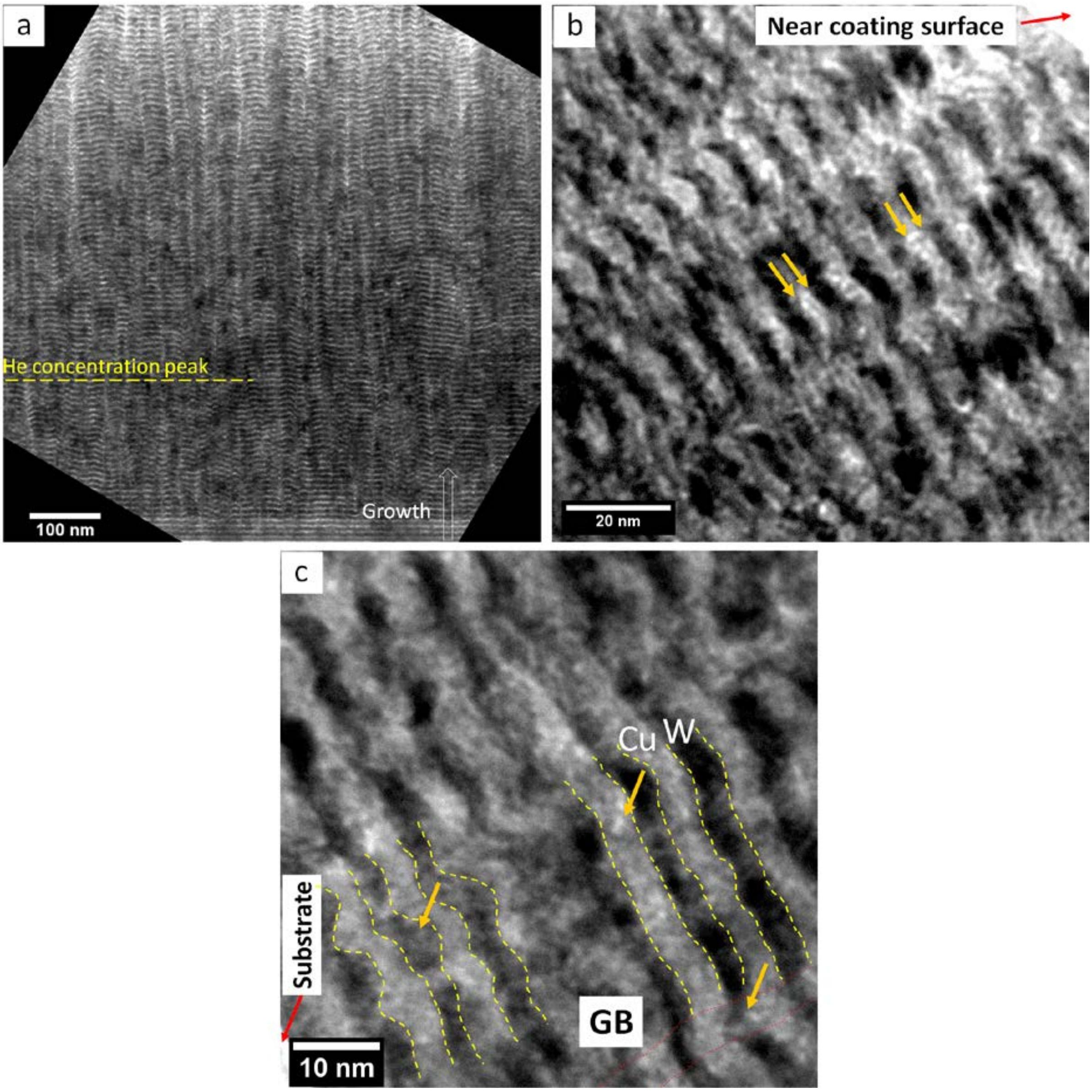
a
He concentration peak
100 nm
Growth
b
Near coating surface
20 nm
c
Cu
W
Substrate
GB
10 nm

Fig. 7

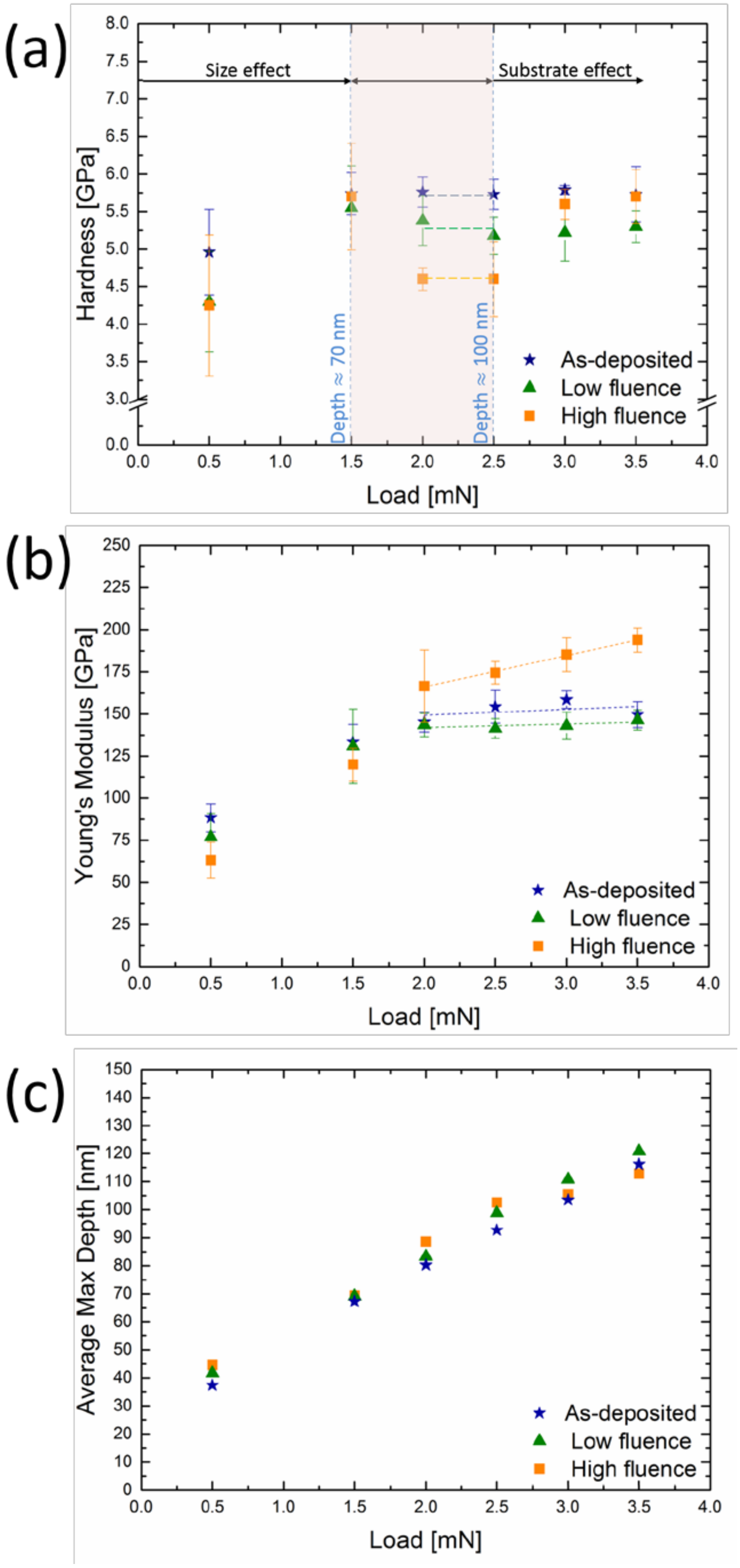
(a)
Size effect
Substrate effect
Depth ≈ 70 nm
Depth ≈ 100 nm
Hardness [GPa]
8.0
7.5
7.0
6.5
6.0
5.5
5.0
4.5
4.0
3.5
3.0
0.0
0.0
0.5
1.0
1.5
2.0
2.5
3.0
3.5
4.0
Load [mN]
As-deposited
Low fluence
High fluence
(b)
Young's Modulus [GPa]
250
225
200
175
150
125
100
75
50
25
0
0.0
0.5
1.0
1.5
2.0
2.5
3.0
3.5
4.0
Load [mN]
As-deposited
Low fluence
High fluence
(c)
Average Max Depth [nm]
150
140
130
120
110
100
90
80
70
60
50
40
30
20
10
0
0.0
0.5
1.0
1.5
2.0
2.5
3.0
3.5
4.0
Load [mN]
As-deposited
Low fluence
High fluence

Fig. 8

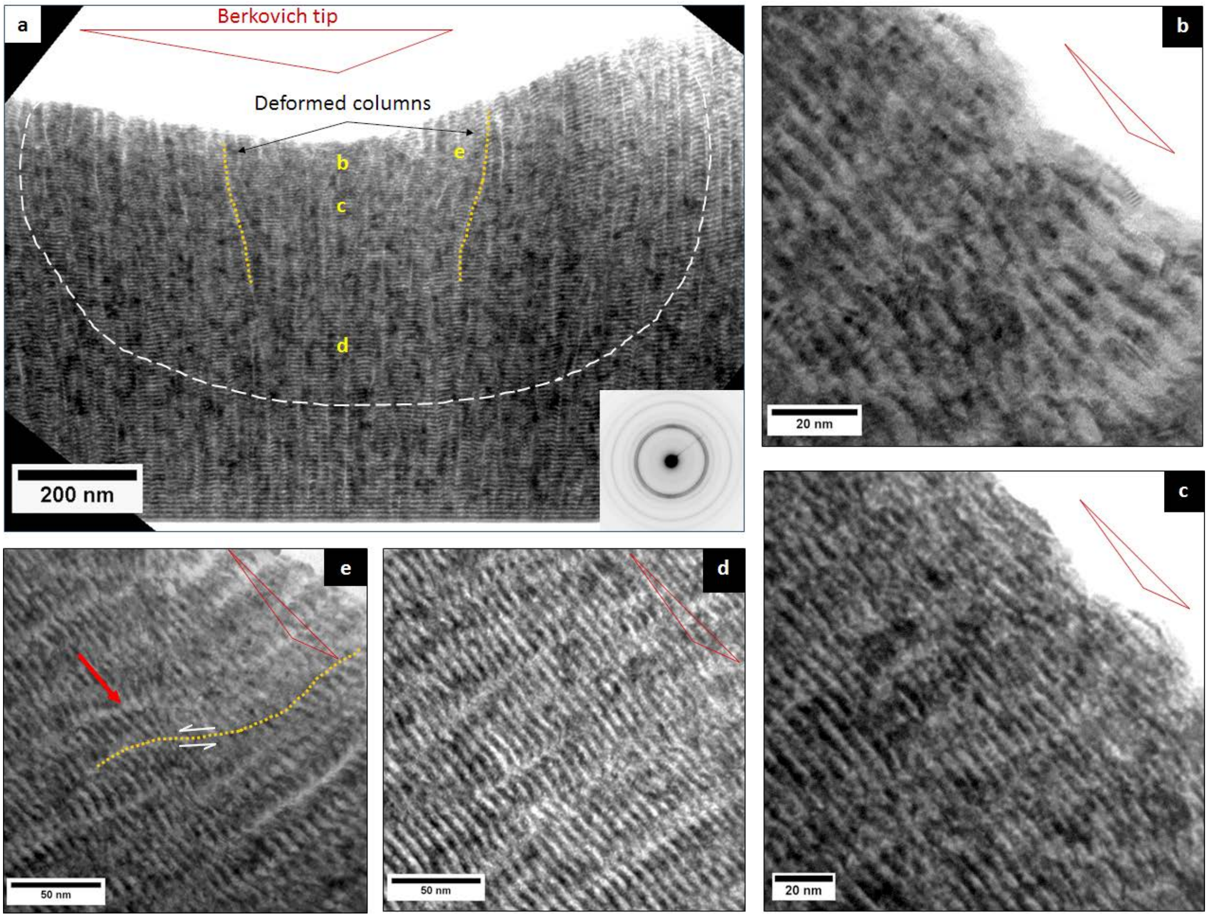
a
Berkovich tip
Deformed columns
b
c
e
d
200 nm
b
20 nm
c
20 nm
e
50 nm
d
50 nm

Fig. 9